HETEROCYCLES, Vol. 83, No. 6, 2011, pp. 1275 - 1290. © The Japan Institute of Heterocyclic Chemistry
Received, 22nd January, 2011, Accepted, 28th March, 2011, Published online, 13th April, 2011
DOI: 10.3987/COM-11-12151

SYNTHESIS, STRUCTURE, AND THEORETICAL CALCULATIONS OF 1*H*-3,7-DIFURYLCYCLOPENTA[3,4-*d*]PYRIDAZINE

Chad A. Snyder,[1]* Nathan C. Tice,[2] Jeremy B. Maddox,[1] Sean Parkin,[3] Aaron W. Daniel,[1] and Jaron M. Thomas[1]

1. Department of Chemistry, Western Kentucky University, Bowling Green, KY 42101-1079, USA, chad.snyder@wku.edu
2. Department of Chemistry, Eastern Kentucky University, Richmond, KY 40475-3102, USA
3. Department of Chemistry, University of Kentucky, Lexington, KY 40506-0055, USA

Abstract – Treating [M{η^5-1,2-$C_5H_3(COC_4H_3O)_2$}$(CO)_3$] (**3**) (M = Mn, **3A**, M = Re, **3B**) with excess hydrazine hydrate in methanol afforded the desired 5,6-fused ring pyridazine complexes, [$M(CO)_3${η^5-1,2-$C_5H_3(CC_4H_3ON)(CC_4H_3ON)$}] (**4**) (M = Mn, **4A**, M = Re, **4B**), in high yield (76%). However, when X-ray crystallographic analysis of the pyridazyl complexes **4A** and **4B** was attempted, all recrystallization trials led to ligand loss to the 1,2-difurylpyridazine, 1,2-$C_5H_3(CC_4H_3ONH)(CC_4H_3ON)$ (**5**). Compound **5** was observed to have a coplanar stacking arrangement in the solid state along the crystallographic b axis. Theoretical calculations performed on compound **5** indicate a high degree of intramolecular electronic delocalization as well intermolecular orbital interaction.

INTRODUCTION

Heterocyclic polymers such as polypyridazine (Figure 1A), polythiophene (Figure 1B), and polypyrrole (Figure 1C) and their organic derivatives have long been of interest for use in electronic materials applications. These types of synthetic polymers have key advantages over traditional inorganic materials, including processability, production cost, and versatility.[1-3] However, to date, polyfuran (Figure 1D) chemistry has been largely unexplored. Unlike pyridazines, thiophenes, and pyrroles, furans have a key advantage in that they can be derived directly and catalytically from biomass.[4,5] Some of these processes are intentional, while others are seen as unwanted by-products or major components in waste streams in the biorefinery sector. For example, the acid-catalyzed depolymerization and

dehydration of cellulose from agricultural or forest activities produces furfural. This industrial process is responsible for a yearly worldwide output of ~ 300,000 tons.[6] Furfural is also utilized for conversion to furfuryl alcohol, which is a precursor to different types of resins and carbonaceous materials.

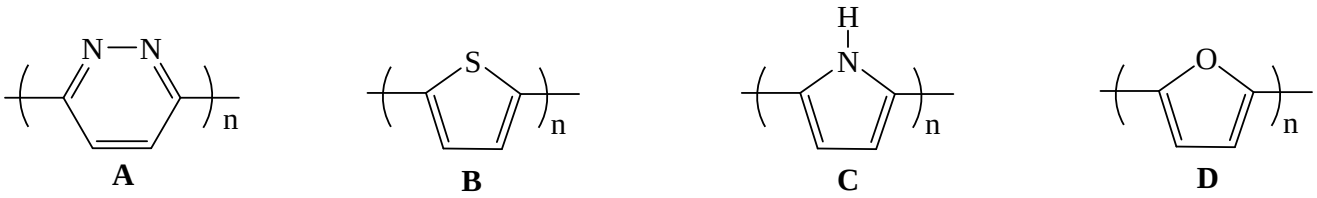

Figure 1. Some heterocyclic polymers for materials applications

Our current work has primarily focused upon facile pathways towards novel pyridazine derivatives that incorporate other heteroatoms in fully aromatic systems. These novel heterocycles are structurally important components of several biologically active compounds and have been explored as α-helix mimetics.[7] Pyridazines have been found to be efficient water oxidation catalysts when compared to dinuclear ruthenium complexes and have shown high efficiencies in catalytic water oxidation having turnover numbers of up to 700.[8] Additionally, pyridazines have been incorporated into iptycene frameworks,[9] compounds researched for polymer sensors,[10] gas absorption storage,[11] and host-guest chemistry.[12] Furthermore, they continue to serve as useful intermediates in the synthesis of several other classes of heterocycles.[13] As part of the full characterization of a general synthesis of furan containing organometallic complexes, $[M(CO)_3\{\eta^5\text{-}1,2\text{-}C_5H_3(CC_4H_3ON)(CC_4H_3ON)\}]$ (**4**), we attempted several recrystallizations only to yield orange-brown, block-like crystals of $1,2\text{-}C_5H_3(CC_4H_3ONH)(CC_4H_3ON)$ (**5**). Herein we report upon the formation, single-crystal X-ray characterization, and electronic studies of 1*H*-3,7-difurylcyclopenta[3,4-*d*]pyridazine (**5**), a unique difuryl substituted pyridazine.

RESULTS AND DISCUSSION

The formation of fused-ring pyridazines has typically been accomplished from a 1,4-diketone or keto-aldehyde aromatic precursor, with benzene or cyclopentadiene (Cp) substrates as those most typically employed.[14-16] Previously, we have had excellent results in forming stable organic and organometallic pyridazine compounds from Cp percursors.[17-19] However, prior to our work, there were no reports of tricarbonyl metal cyclopenta[*c*]pyridazyl complexes that incorporate furyl substituents. We envision manganese and rhenium 1,4-difurylcyclopenta[*c*]pyridazyl complexes (Scheme 1, **4**) having a large potential for utilization in electronic materials (*e.g.*, solar cells) using the reported alkyl and aryl thiophene and pyridazine chemistry as a synthetic guide.[2,3,18] These fused heterocycles will serve as synthetic models and building blocks for potential organic or organometallic conducting polymers. In addition, those materials that incorporate furan derivatives will have the added benefit of incorporating renewable feedstocks into the electronic framework.

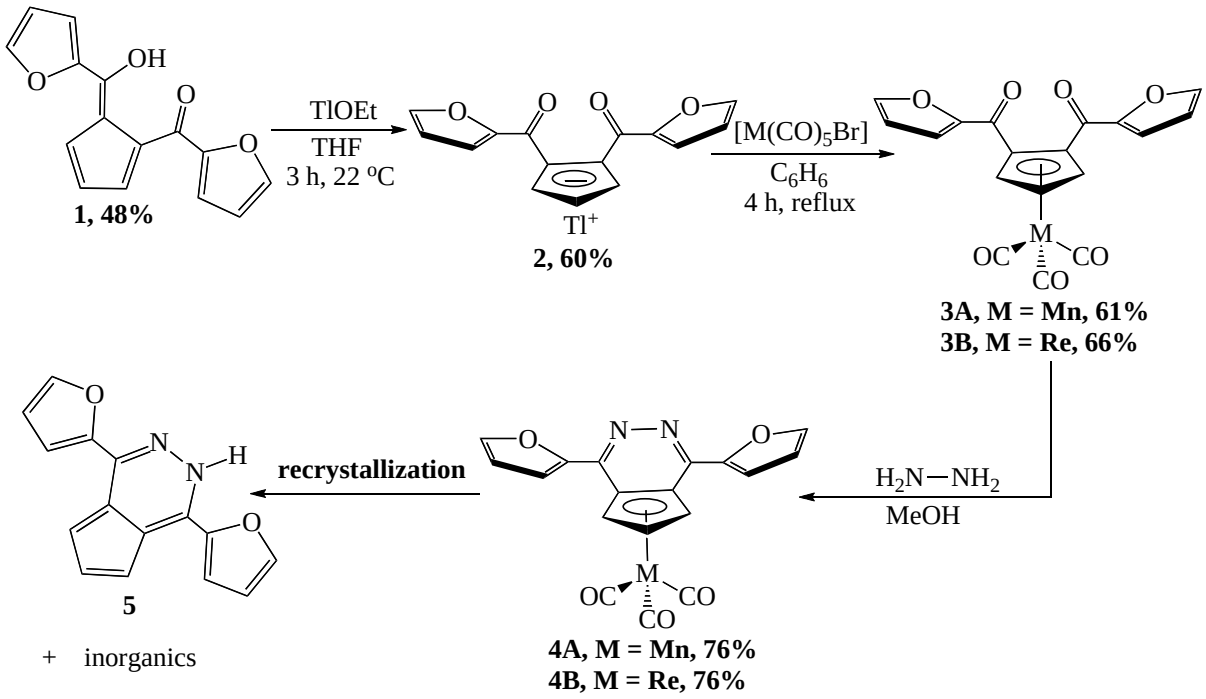

Scheme 1. Synthesis of and formation of 1*H*-3,7-difurylcyclopenta[3,4-*d*]pyridazine (**5**)

Complexes **3–4** were synthesized in good yields (61–76%) and fully characterized, as previously reported.[20] All attempts in obtaining single crystals for x-ray analysis of **4A–B** resulted in ligand loss to pyridazine **5**. The structure of compound **5** was confirmed by NMR, IR, and MS analysis and matched the values we previously reported from the direct ligand synthesis of pyridazine **5** from fulvene from 1,2-$C_5H_3(COC_4H_3O)(COHC_4H_3O)$ (Figure 2).[17]

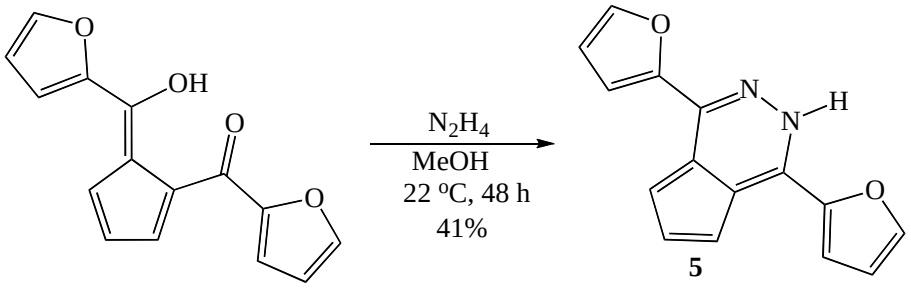

Figure 2. Direct ligand **5** synthesis from 1,2-$C_5H_3(COC_4H_3O)(COHC_4H_3O)$

NMR spectral analysis confirms the ligand loss of complexes **4A** and **4B** to pyridazine **5**. Protonation to afford the free ligand was most likely due to residual methanol or water contamination in the solvent. The furyl rings protons are observed as a doublet of doublets (δ 6.66, 1H, $^3J_{AB}$ = 3.5 Hz, $^3J_{AC}$ ß= 1.7 Hz, CHC*H*CHO), a doublet (δ 7.33, 1H, ^3J = 3.5 Hz, C*H*CHCHO), and a multiplet (δ 7.66, 2H). The Cp ring protons were observed as a doublet (δ 7.25, 2H, ^3J = 4.0 Hz, C*H*CHC*H*) and a triplet (δ 7.53, 1H, ^3J

= 4.0 Hz, CHC*H*CH), which is typical of this class of compounds. Finally, the amine proton was shown as a broad singlet at 11.2 ppm, which is the expected range for the delocalized amine proton in NMR solvent solution. The ^{13}C NMR of **5** displayed Cp carbon signals at δ 108.5 (*C*HCH*C*H) and 112.4 (CH*C*HCH), while the C=N signal was observed downfield at 144.3 ppm. The distinct resonances at 222.3 and 221.6 ppm corresponding to the metal carbonyls for complexes **4A** and **4B** were absent for **5**. Mass spectrometry also confirms the molecular weight of **5**, with both the base and M^+ peaks at 250 *m/z*. Again, there was no evidence of the tricarbonyl metal moiety in the mass spectrum. IR spectroscopy also showed evidence of the formation of the C=N double bond (1612 cm^{-1}), with loss of the carbonyl stretches observed in complexes **4A** and **4B** (1890-2029 cm^{-1}). The structure of pyridazine **5** was also confirmed by X-ray crystallographic analysis (Figure 3).

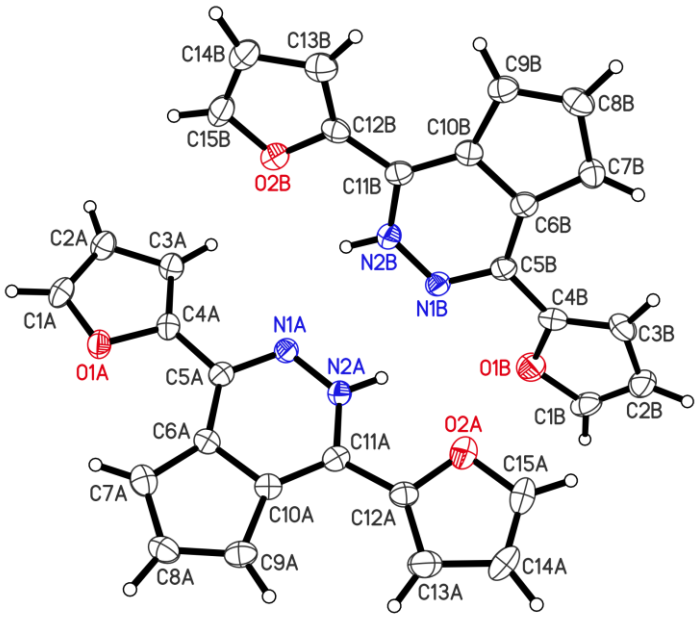

Figure 3. Molecular structure of pyridazine **5** with 50% probability of ellipsoid plots

Compound **5** crystallizes in the monoclinic space group, *P* 2_1 with two molecules in the asymmetric unit. (distinguished as "A" and "B"). The furyl rings for molecule A are anti-periplanar with respect to each other and nearly coplanar to the central pyridazine ring, with the dihedral angles for [C3A–C4A–C5A–N1A] and [N2A–C11A–C12A–O2A] being 4.6(5)° and 9.7(4)°, respectively. In contrast, the furyl rings for molecule B are syn-periplanar with respect to each other and nearly coplanar to the central pyridazine ring, with the dihedral angles for [N2B–C11B–C12B–O2B] and [O1B–C4B–C5B–N1B] at -8.3(4)° and 13.2(4)°, respectively. The central pyridazyl Cp ring is highly planar, with the root-mean-square deviation from the planes created by N1, N2, C5–C12 in molecules A and B at 0.006(2) Å and 0.014(2) Å, respectively. The imine carbon bond lengths, N1A–C5A and

N1B–C5B, are relatively equidistant at 1.340(4) and 1.329(4) Å, respectively. The Cp ring average bond length (C6A–C7A; C7A–C8A; C8A–C9A; C9A–C10A) is 1.402(9) Å, with the C6A–C10A bond length significantly longer (1.465(4) Å) compared to the other four Cp bonds. The C=C bonds within the furan portion of **5** are significantly shorter than those in the pyridazine ring. For example, the bond lengths for C1A–C2A and C3A-C4A are 1.347(4) and 1.359(4) Å, respectively, compared to those of C6-C7A (1.400(4) Å) and C9-C10A (1.410(4) Å). This observation most likely reflects the furan delocalized π system versus the non-aromatic Cp ring. A pair of hydrogen bonds link the amine groups of each unique molecule (N2A–H2NA and N2B–H2NB) and the imine nitrogen on the adjacent molecule (N1A and N1B), with hydrogen bond distances (N1….H2N) at 2.886(3) and 2.961(3) Å, respectively. This causes an inverted arrangement for each unique molecule with respect to the other, with the furyl ring that contains O1A in molecule A adjacent to the furyl ring that contains O2B in molecule B.

Analysis of compound **5** does show some π–stacking in the solid state. For molecule A, the adjacent stacked molecule, generated by the (x,y,z) to (x, y-1, z) transformation, is arranged "face-to-face" and slightly offset. This planar arrangement can be best observed along the crystallographic b axis (Figure 4). The pyridazyl portion within one layer is aligned with the furyl ring of the adjacent layer (Figure 5, top). A short contact (a distance less than the sum of the Van der Waals radii) is observed between C15A and N1A (3.245 Å). Furthermore, other analogous distances between the stacked layers are well within the commonly accepted values (3.4 to 3.6 Å) for evidence of π–stacking (e.g., C3A to N2A is 3.381 Å).[21] Planes created by adjacent layers of molecule A also indicate a high degree of π–stacking, with an inter-planar distance of 3.355 Å. By contrast, while molecule B does display a coplanar stacking arrangement between layers, the relative molecule placement is very different (Figure 5, bottom). There is far less evidence of π–orbital overlap as compared to the arrangement for molecule A, and no short contacts are observed between adjacent layers of molecule B. While there does appear to be some evidence of π–π interaction (e.g., with the distance between C8B and O2B is 3.3376 Å) the interlayer distances between most atoms are too far for orbital overlap to occur. This is not due to the actual distance between the stacked layers of molecule B (the distance calculated between those two planes created by B is 3.273 Å). Instead, it is a greater displacement between these stacked molecules in molecule B that makes the actual amount of π–interaction weak. Only the Cp portion of one layer and the furyl ring containing O2B of the adjacent layer have any significant overlap for molecule B.

Tables of crystallographic details, atomic coordinates and displacement parameters, bond distances and angles, intermolecular contact distances, structure factors and a crystallographic information file (CIF) for the structure of **5** have been deposited with the Cambridge Crystallographic Data Centre.[22]

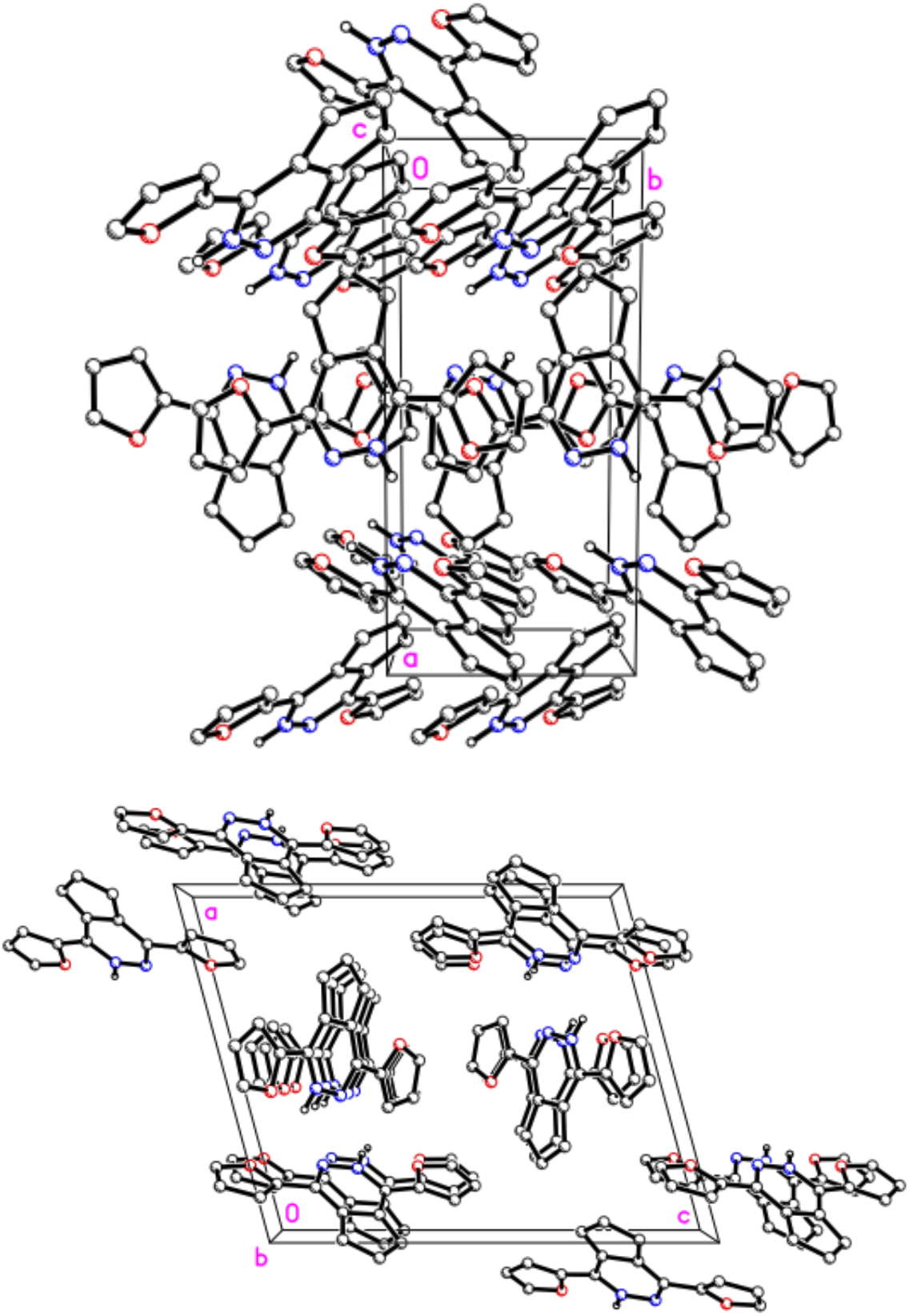

Figure 4. Molecular packing of **5** along the c and b crystallographic axis, respectively

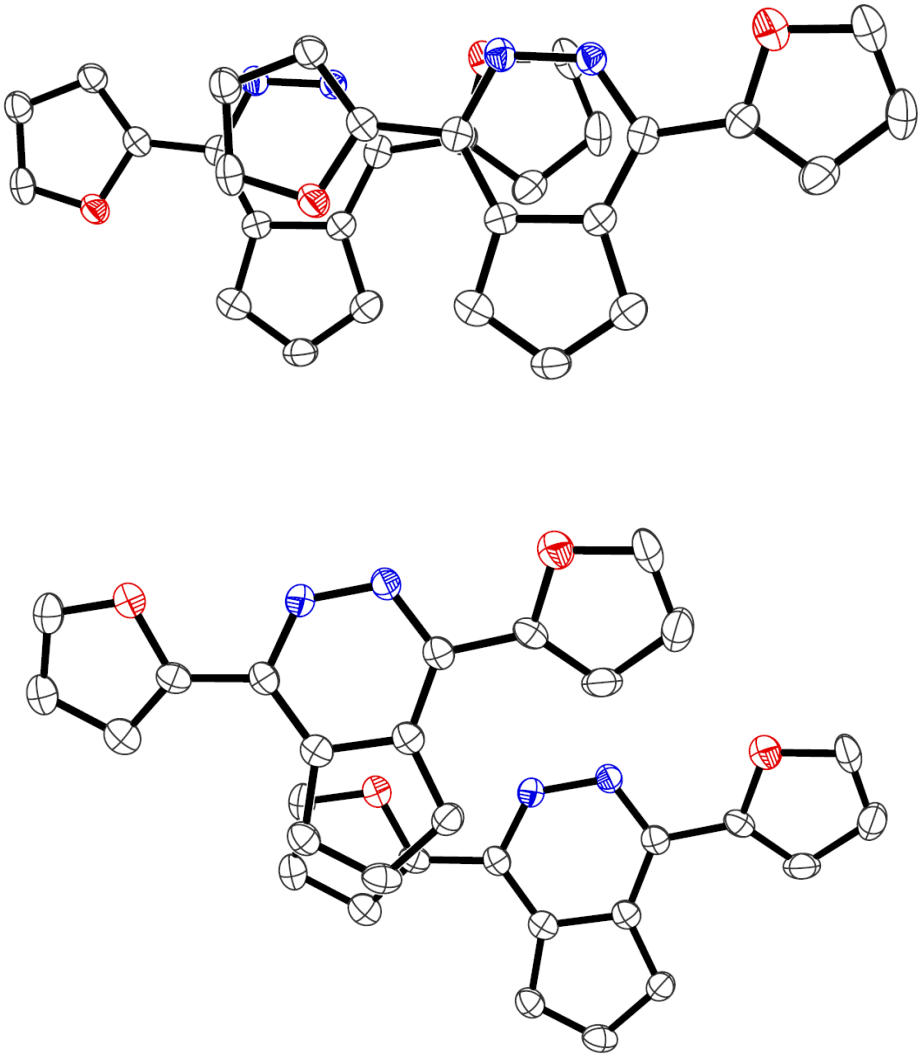

Figure 5. View of the molecular packing of molecule A (top) and molecule B (bottom) generated by the transformation (x, y, z) to (x, y-1, z)

To further characterize the molecular geometry and electronic structure of compound **5** we have performed a variety of quantum chemistry calculations. These have been carried out using density functional theory (DFT) methods as implemented within the Gaussian 09 electronic structure package.[23] We have constructed several molecular and bi-molecular configurations of compound **5** using the x-ray crystal structure data. These include the unique conformers A and B and three dimers, which are representative of the A–A, B–B, and A–B bi-molecular configurations. For each configuration we have performed a single point energy DFT calculation using the Perdew-Burke-Ernzerhof (PBE) generalized gradient exchange-correlation functional[24] and a triple-zeta correlation consistent basis set (cc-pVTZ).[25] We also obtained optimized molecular geometries and performed a vibrational frequency analysis for the isolated molecules A and B using a double-zeta basis set (cc-pVDZ).

The geometry optimization for molecule A yielded a nearly planar configuration, where the dihedral angles [C3A–C4A–C5A–N1A] and [N2A–C11A–C12A–O2A] relaxed to -0.004° and 0.069°, respectively. In contrast, molecule B relaxed to a more non-planar configuration; the dihedral angles [N2B–C11B–C12B–O2B] and [O1B–C4B–C5B–N1B] were found to be 4.92° and -17.60°, respectively. The relaxed molecule A was found to be 0.08 eV lower in energy compared to molecule B. It was found that the imine carbon bond lengths increased in the relaxed geometries, such that [N1A–C5A] and [N1B–C5B] were 1.3484Å and 1.3464Å, respectively. Similarly, the bond lengths in the Cp ring also increased upon relaxation. The average Cp bond length was found to be 1.4135Å, and the [C6A–C10A] bridging bond length (1.4804Å) was found to be larger than the average; this is qualitatively consistent with the crystal structure data. After optimization, the variation of the C=C bond lengths between the furyl and pyridazine ring are also found to be qualitatively consistent with the crystal structure. The bond lengths for the relaxed furyl C=C bonds [C1A–C2A] and [C3A–C4A] were 1.3761Å and 1.3848Å, respectively, and the Cp ring C=C bond [C6A–C7A] and [C9A–C10A] were 1.4066Å and 1.4157Å, respectively.

In Figure 6(I), we illustrate the theoretical charge density (PBE/cc-pVTZ) and electrostatic potential maps for the isolated molecules A and B, and the three dimers A–A, B–B, and A–B. The 3D charge density for each molecular configuration is represented by a single surface contour (isovalue 0.004) that indicates the spatial extent of the molecule's total charge density. The charge density contour is further color-coded with the value of the electrostatic potential (between -0.05 and +0.05). Red coloring indicates a lower value electrostatic potential and corresponds to electron-rich regions of the molecule, while blue coloring represents a higher electrostatic potential associated with electron-deficient regions. The electrostatic potential maps for molecular configurations A and B are shown on the top-left and top-right, respectively. These figures show electron-rich regions associated with the lone pairs on the furyl oxygen atoms and imine nitrogen atoms. This is particularly noticeable in molecule B, where the furyl oxygen and imine nitrogen are in close proximity. In contrast, the amine group is electron-deficient, which is likely related to the low occupancy of the lone pairs on N2A and N2B. In addition, the Cp region for each molecule displays an increased degree of electron density as compared to the corresponding furyl carbons. This observation is similar to that found on the furyl containing manganese and rhenium metallocenes we previously reported upon.[20] The center graphic of Figure 6(I) shows the charge density and potential map for the A–B dimer. The electron-rich and electron-deficient regions of the pyridazine-furyl moieties are precisely paired by the inverted configuration of the two molecules, in a "jig-saw" arrangement, such that the magnitude of the potential is decreased in the region of the intermolecular hydrogen bond contacts. The charge density and potential maps for the A–A and B–B dimers are shown in the lower left and right portions of Figure 6(I), respectively.

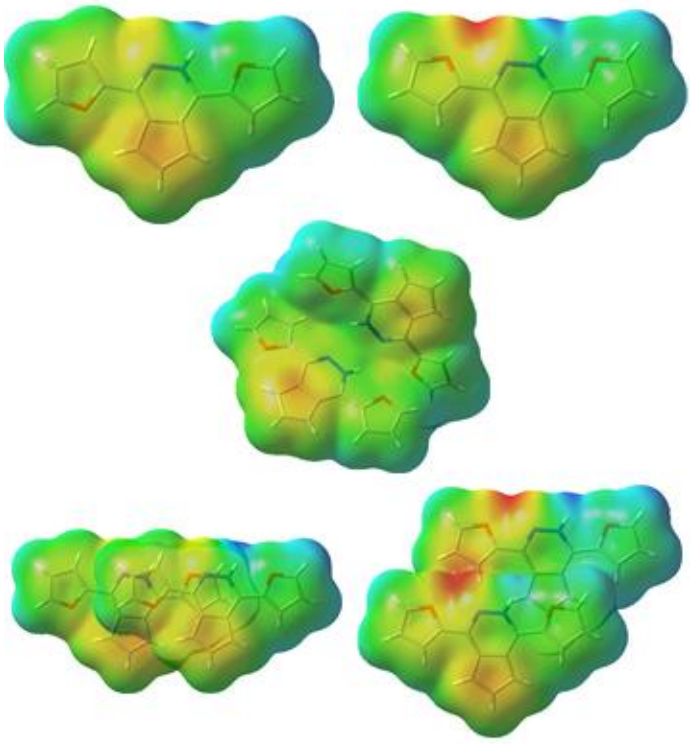

I

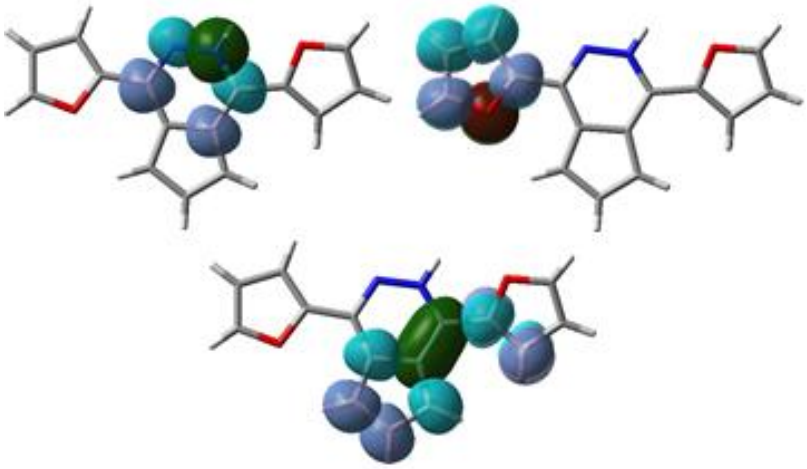

II

Figure 6. Charge density contours (isovalue 0.004) and electrostatic potential maps (-0.05 to 0.05) for various molecular configurations (I) and selected natural bonding orbitals for molecule A (II)

In both cases we have adjusted the viewing angle, such that the pyridazine-Cp rings are planar with respect to the page. There is some overlapping charge density for both the A–A and B–B

configurations; however, the alignment of the A–A dimer appears to have greater overlap compared with the B–B configuration.

To help understand the electronic structure more quantitatively, we have performed an electronic population analysis for the monomeric and various dimer configurations using the natural bond orbital (NBO) approach.[26,27] To keep the NBO analysis for compound **5** tractable, we have repeated the DFT calculations for all crystal structure configurations using a smaller and more manageable 3-21G basis set. The NBO analysis of molecules A and B confirm that the electronic structures for these systems are highly delocalized. Compound **5** has a total of 130 electrons and the population analysis predicts that 126.3 electrons occupy Lewis-type core and bonding orbitals, and that 2.73% (roughly 3.5 electrons) are populating non-Lewis-type, anti-bonding orbitals. Of particular importance is the fact that the lone pair orbitals associated with the furyl oxygens and the amino nitrogen atom on pyridazine have significantly less than full population (e.g., 1.53 for the amine nitrogen on molecule A). These orbitals act as electron donors that are strongly coupled (~23-38 kcal/mol) with C=C (or N=C in the case of the amino N lone pair) anti-bonding orbitals, which act as electron acceptors. Examples of the NBOs involved in this coupling are shown in the top-left and top-right illustrations of Figure 6(II). Donor lone pair valence orbitals are shown as the red/green surface contours (isovalue of 0.05). The blue/purple surfaces correspond to the anti-bonding acceptor orbitals. Note that two acceptor orbitals are shown for each donor. For the top-left case, we observe that a low occupancy lone pair on the imine nitrogen couples to N=C and C=C anti-bonds in the pyridazine ring. In the top-right illustration of Figure 6(II), we observe that a low occupancy lone pair on the furyl ring couples to C=C anti-bonding orbital. The bottom illustration of Figure 2 shows a C=C bonding NBO that is strongly coupled (11-14 kcal/mol) to a pair of C=C anti-bonding orbitals in the Cp ring system and a C=C anti-bonding furyl orbital. We also observe that several additional anti-bonding orbitals have significant populations (on the order 0.27-0.43 electrons); these are in turn coupled to other anti-bonding orbitals within pyridazine ring system (not illustrated), which provides further indication that the electronic system of compound **5** is highly delocalized.

In Figure 7, selected NBOs for the A–A, B–B, and A–B bi-molecular configurations are displayed. It should be noted that the intramolecular NBOs described above and shown in Figure 6(II) are also found within dimer pairs. However, the primary focus of our analysis on the intermolecular couplings is between NBOs on different molecular units. Generally, we see that the couplings between NBOs on different molecules are much smaller compared to intramolecular coupling. The top-left and top-right illustrations of Figure 7 show several NBOs for the A–A dimer configuration. On the top-left, two coupled pairs of NBOs are displayed: a lone pair valence orbital on the amine nitrogen atom of the upper unit is coupled (0.22 kcal/mol) to a C=C anti-bonding orbital on the underlying furyl ring, which acts as

an electron acceptor. Also shown is a C=C bonding orbital that couples (0.24 kcal/mol) to the imine N=C anti-bonding orbital of the lower pyridazine ring. A similar set of NBOs are illustrated in the top-right of Figure 7. However, in contrast to the previous NBOs, these lead to charge transfer from the lower unit to the upper unit. We note that there are several other pairs of NBOs that couple the two molecular units. The charge transfer is fairly balanced between the pair in that there is only a very small net charge transfer (0.00125 electrons) from the upper to lower unit. The center illustration shows the most strongly coupled NBOs for the A–B dimer and are associated with the two hydrogen bonds between these units. These NBOs consist of lone pair donors on the imine nitrogens that couple to the amine N-H anti-bonding orbitals on the adjacent molecule. The two hydrogen bonds are not equivalent, and our calculations show that the [N1A–H–N2B] NBO coupling is 3.6 kcal/mol and that the [N1B–H–N2A] NBO coupling is 6.01 kcal/mol. This makes sense in light of the fact that the two hydrogen bonding geometries are not equivalent. The weaker bond has a longer N…H distance; 2.3184 Å for [N1A…H] versus 2.14662 Å for [N1B…H]. Also, the [N1A…H–N2B] bond angle is more acute than the [N1B…H–N2A] angle by 10°. The difference between the two hydrogen bonds leads to a larger amount of charge transfer (0.00961 electrons) from molecule A to molecule B. As expected, there are fewer pairs of strongly coupled NBOs between the B-B molecular units compared to the A–A and A–B dimers. The orbitals that do couple strongly (~0.2 kcal/mol) are located on the Cp ring of the upper unit and the furyl ring of the lower unit. These are shown in the lower-left and lower-right illustrations of Figure 7.

The NBO analysis illustrates that intramolecular electronic delocalization is particularly strong for compound **5**. In particular, lone pair orbitals on the oxygen atoms of the furyl rings and amino nitrogen of the pyridazine group exhibit low occupancy, while several carbon-carbon anti-bonding orbitals show high occupancy; moreover, many of these orbitals are strongly coupled to adjacent anti-bonding orbitals within a given molecular unit. The intermolecular electronic coupling is somewhat weaker compared to the intramolecular coupling; however, it is still significant. Our analysis of the A–A, B–B, A–B dimer configurations shows that the hydrogen bonds between neighboring pyridazine units in the A-B arrangement are by far the strongest interactions. Electronic coupling between A–A and B–B units is smaller but non-negligible. The different bi-molecular arrangements of the A–A and B–B dimers lead to couplings between different parts of the molecules. The A–A dimer interactions act between orbitals of the furan ring of one unit and the pyridazine system of the other, while in the B-B dimer the interactions occur through the furan and Cp rings on different molecular units. Overall, the NBO analysis confirms our conclusion from the solid state data that the interaction between A–A molecular pairs is much stronger versus the B–B pairs, as shown by the greater orbital overlap between adjacent structures.

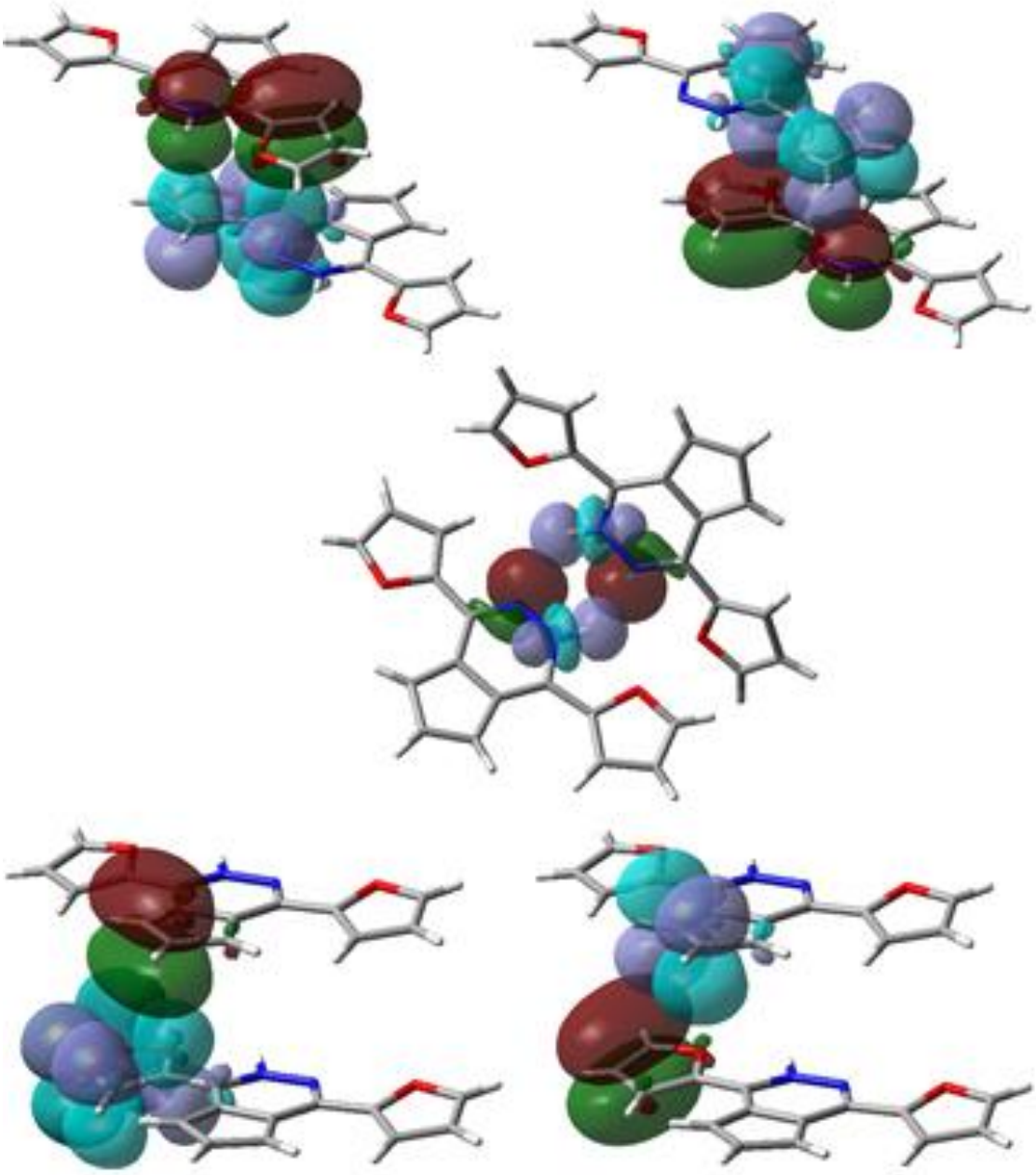

Figure 7. Selected donor-acceptor NBOs for several dimer configurations of compound 5

EXPERIMENTAL

General Procedures. All reactions were carried out using standard Schlenk techniques under a nitrogen atmosphere unless otherwise noted. NMR solvent $CDCl_3$ (Aldrich) was used without further purification. Hydrazine hydrate, MeOH, magnesium sulfate, Et_2O, CH_2Cl_2, acetone, hexane, and $[Mn\{\eta^5\text{-}1,2\text{-}C_5H_3(COC_4H_3O)_2\}(CO)_3]$ (**3A**) and $[Re\{\eta^5\text{-}1,2\text{-}C_5H_3(COC_4H_3O)_2\}(CO)_3]$ (**3B**) were also used without further purification.

^{1}H and ^{13}C NMR spectra were recorded on a JEOL-500 MHz NMR spectrometer at ca. 22 ^{o}C and were referenced to residual solvent peaks. All ^{13}C NMR spectra were listed as decoupled. Infrared spectra were recorded on Spectrum One FT-IR Spectrometer. Electron ionization (EI) mass spectra were recorded at 70 eV on a Perkin Elmer GC/MS. Melting points were taken on a standard Mel-Temp apparatus. X-Ray diffraction data were collected at 90 K on a Nonius KappaCCD diffractometer at the University of Kentucky X-Ray Crystallographic Laboratories. Elemental analysis was performed at Atlantic Microlabs, Inc. in Norcross, GA.

Synthesis of 1,2-$C_5H_3(CC_4H_3ONH)(CC_4H_3ON)$ (5) To a 20 mL round-bottom flask, [Mn{η^5-1,2-$C_5H_3(COC_4H_3O)_2$}$(CO)_3$] (**3A**, 250 mg, 0.255 mmol) was dissolved in 10 mL of MeOH. An excess of hydrazine hydrate (1.00 mL, 1.03 g, 20.6 mmol) was then added to the solution. The solution was stirred 24 h at room temperature. To the reaction mixture, water (20 mL) was added and a red precipitate formed immediately. The aqueous suspension was washed with Et_2O (3 x 5 mL) and the organic layers were collected, dried ($MgSO_4$), and filtered. The volatiles were removed *in vacuo* and the crude product was triturated with cold hexane to give [$Mn(CO)_3${η^5-1,2-$C_5H_3(CC_4H_3ON)(CC_4H_3ON)$}] (**4A**, 188 mg, 0.0644 mmol, 75.6%) as a red-orange powder. Recrystallization of **4A** from a variety of solvents (*e.g.*, acetone, CH_2Cl_2, Et_2O) yielded only 1,2-$C_5H_3(CC_4H_3ONH)(CC_4H_3ON)$ (**5**). A similar reaction that produced [$Re(CO)_3${η^5-1,2-$C_5H_3(CC_4H_3ON)(CC_4H_3ON)$}] (**4B**, 151 mg, 0.290 mmol, 76%) from [Re{η^5-1,2-$C_5H_3(COC_4H_3O)_2$}$(CO)_3$] (**3B**, 200 mg, 0.382 mmol) and excess of hydrazine hydrate (1.00 mL, 1.03 g, 20.6 mmol) also yielded pyridazine **5** after several recrystallization attempts. **Mp** 146–148 ^{o}C. **^{1}H NMR (500 MHz, $CDCl_3$, ppm)**: δ 6.66 (dd, 1H, $^{3}J_{AB}$ = 3.5 Hz, $^{3}J_{AC}$ = 1.7 Hz CHC*H*CHO), 7.25 (d, 1H, ^{3}J = 4.0 Hz, C*H*CHCH), 7.33 (d, 1H, ^{3}J = 3.5 Hz, C*H*CHCHO), 7.53 (t, 1H, ^{3}J = 4.0 Hz, CHC*H*CH), 7.66 (m, 2H, Fr), 11.2 (br s, 1H, NH). **^{13}C NMR (125 MHz, $CDCl_3$, ppm**): δ 108.5 (*C*HCH*C*H), 112.4 (CH*C*HCH), 112.7 (NC*C*CH), 112.6, 118.0, 133.2 (Fr) 144.3 (CHCH*C*N). **IR (KBr, cm^{-1})**: 1612 (CN), 2958 (C–H), 3240 (N–H). **MS**: *m/z* 250 (M^+ and base peak), 221 (M^+– CHO), 193 ($M^+ – C_2H_2O_2$). Anal Calcd. for $C_{15}H_{10}N_2O_2$: C, 71.99; H, 4.03. Found: C, 74.32; H, 6.30.

The X-ray crystallographic structure of **5** was determined by X-ray crystallographic methods. The crystals for which data were collected were typical of others in the batch, which had been grown by slow evaporation from methylene chloride at room temperature. These crystals were mounted on glass fibers with polyisobutene oil. Data were collected at 90 K on a Nonius KappaCCD diffractometer. The main programs used were from the Denzo-SMN package for indexing, data reduction and absorption correction,[28] SHELXS-97 for structure solution, and SHELXL-97 for refinement.[29] Hydrogen atoms were placed in geometrically calculated positions. Crystal data and a summary of experimental details are given in Table 1.

Table 1. Crystal Data and Structure Refinement for 1*H*-3,7-difurylcyclopenta[3,4-*d*]pyridazine

Empirical formula	$C_{15}H_{10}N_2O_2$
Formula weight	250.25
Temperature	90.0(2) K
Wavelength	0.71073 Å
Crystal system	Monoclinic
Space group	$P\,2_1$
Unit cell dimensions a = 12.8754(2) Å b = 5.90380(10) Å c = 15.5817(2) Å	 $\alpha = 90^\circ$ $\beta = 105.0649(6)^\circ$ $\gamma = 90^\circ$
Volume	1143.72(3) $Å^3$
Z, Calculated density	4, 1.453 Mg/m^3
Absorption coefficient	0.099 mm^{-1}
F(000)	520
Crystal size	0.20 x 0.18 x 0.06 mm
θ range for data collection Limiting indices	1.35 to 27.47° -16<=h<=16, -7<=k<=7, -20<=l<=20
Reflections collected/unique	26530 / 2887 [R(int) = 0.0630]
Completeness to θ = 68.73	100.0 %
Absorption correction	Semi-empirical from equivalents
Max. and min. transmission	0.994 and 0.981
Refinement method	Full-matrix least-squares on F^2
Data/restraints/parameters	2887/1/343
Goodness-of-fit on F^2	1.053
Final *R* indices [I>2σ(I)]	*R1* = 0.0472, *wR2* = 0.1135
R indices (all data)	*R1* = 0.0747, *wR2* = 0.1267
Largest diff. peak and hole	0.300 and -0.259 $e.Å^{-3}$

ACKNOWLEDGEMENTS

We would like to acknowledge our sources of financial support, including Western Kentucky University's Chemistry Department, their Office of Sponsored Programs, their Faculty Scholarship

Council, and the WKU Advanced Materials Institute. Additional sources of support include Eastern Kentucky University's Center for Renewable and Alternative Fuel Technology (CRAFT), the Chemistry Diversity Initiative, the University Research Committee, and their Department of Chemistry. JBM gratefully acknowledges the support of the Applied Research and Technology Program (ARTP) at WKU.

REFERENCES AND NOTES

1. G. Zotti and B. Verchelli, *Acc. Chem. Res.*, 2008, **41**, 1098.
2. A. R. Katritzky and C. W. Rees, 'Comprehensive Heterocyclic Chemistry: Structure, Reactions, Synthesis and Uses of Heterocyclic Xompounds,' Pergamon Press: Oxford, 1984.
3. J. Roncali, *Chem. Rev.*, 1997, **97**, 173.
4. H. B. Zhao, J. E. Holladay, H. Brown, and Z. C. Zhang, *Science*, 2007, **316**, 1597.
5. Y. Roman-Leshkov, C. J. Barrett, Z. Y. Liu, and J. A. Dumesic, *Nature*, 2007, **447**, 982.
6. A. Gandini, *Macromolecules*, 2008, **41**, 9491.
7. A. Volonterio, L. Moisan, and J. Rebek, Jr., *Org. Lett.*, 2007, **9**, 3733.
8. Y. Xu, T. Akermark, V. Gyollai, D. Zou, L. Eriksson, L. Duan, R. Zhang, B. Akermark, and L. A. Sun, *Inorg. Chem.*, 2009, **48**, 2717.
9. J. Bouffard, R. F. Eaton, P. Muller, and T. M. Swager, *J. Org. Chem.*, 2007, **72**, 10166.
10. J. S. Yang and T. M. Swager, *J. Am. Chem. Soc.*, 1998, **120**, 5321.
11. B. S. Ghanem, K. J. Msayib, N. B. McKeown, K. D. M. Harris, Z. Pan, P. M. Budd, A. Butler, J. Selbie, D. Book, and A. Walton, *Chem. Commun.*, 2007, 67.
12. T. Han, Q. S. Zong, and C. F. Chen, *J. Org. Chem.*, 2007, **72**, 3108.
13. G. P. Ellis, 'Synthesis of Fused Heterocycles,' John Wiley and Sons Inc.: New York, 1987.
14. A. G. J. Anderson and D. M. Forkey, *J. Am. Chem. Soc.*, 1969, **91**, 924.
15. K. Hafner, H. E. A. Kramer, H. Musso, G. Ploss, and G. Schultz, *Chem. Ber.*, 1964, **97**, 2066.
16. W. J. Linn and W. H. Sharkey, *J. Am. Chem. Soc.*, 1957, **79**, 4970.
17. C. A. Snyder, N. C. Tice, P. G. Sriramula, J. L. Neathery, J. K. Mobley, C. L. Phillips, A. Z. Preston, J. M. Strain, E. S.Vanover, M. P. Starling, N. V. Sahi, and K. R. Bunnell, *Synth. Commun.*, 2010, *manuscript accepted*.
18. N. C. Tice, 'The Synthesis, Structure, and Reactivity of Some Organometallic-Fused Heterocycles,' Ph.D. Thesis, Department of Chemistry, University of Kentucky, Lexington, KY, 2006.
19. N. C. Tice, S. M. Peak, and S. Parkin, *Heterocycles*, 2010, **81**, 1631.
20. C. A. Snyder, N. C. Tice, J. B. Maddox, E. D. Emberton, E. S. Vanover, D. F. Hinson, and D. C. Jackson, *J. Organomet. Chem.*, 2011, *in press, accepted manuscript*.
21. M. D. Curtis, J. Cao, and J. W. Kampf, *J. Am. Chem. Soc.*, 2004, **126**, 4318.
22. CCDC 806631 contains the supplementary crystallographic data for this paper. These data can be

obtained free of charge from The Cambridge Crystallographic Data Centre via www.ccdc.cam.ac.uk/data_request/cif.

23. M. J. Frisch, G. W. Trucks, H. B. Schlegel, G. E. Scuseria, M. A. Robb, J. R. Cheeseman, G. Scalmani, V. Barone, B. Mennucci, G. A. Petersson, H. Nakatsuji, M. Caricato, X. Li, H. P. Hratchian, A. F. Izmaylov, J. Bloino, G. Zheng, J. L. Sonnenberg, M. Hada, M. Ehara, K. Toyota, R. Fukuda, J. Hasegawa, M. Ishida, T. Nakajima, Y. Honda, O. Kitao, H. Nakai, T. Vreven, J. A. Montgomery, Jr., J. E. Peralta, F. Ogliaro, M. Bearpark, J. J. Heyd, E. Brothers, K. N. Kudin, V. N. Staroverov, R. Kobayashi, J. Normand, K. Raghavachari, A. Rendell, J. C. Burant, S. S. Iyengar, J. Tomasi, M. Cossi, N. Rega, N. J. Millam, M. Klene, J. E. Knox, J. B. Cross, V. Bakken, C. Adamo, J. Jaramillo, R. Gomperts, R. E. Stratmann, O. Yazyev, A. J. Austin, R. Cammi, C. Pomelli, J. W. Ochterski, R. L. Martin, K. Morokuma, V. G. Zakrzewski, G. A. Voth, P. Salvador, J. J. Dannenberg, S. Dapprich, A. D. Daniels, Ö. Farkas, J. B. Foresman, J. V. Ortiz, J. Cioslowski, and D. J. Fox, Gaussian, Inc., Gaussian 09, Revision **A.1**, Wallingford CT, 2009.
24. J. P. Perdew, K. Burke, and M. Ernzerhof, *Phys. Rev. Lett.*, 1996, **77**, 3865.
25. T. H. Dunning Jr., *J. Chem. Phys.*, 1989, **90**, 1007.
26. NBO Version 3.1, E. D. Glendening, A. E. Reed, J. E. Carpenter, and F. Weinhold.
27. The NBO population analysis can be qualitatively understood as a reorganization of the electronic structure into a set of high occupancy Lewis-type one-center or two-center orbitals that may be categorized as core, bonding, and lone pair orbitals. Similarly, a set of low occupancy non-Lewis-type Rydberg and anti-bonding orbitals are also found. This analysis does not affect the approximate wave function (or rather charge density, in the case of DFT) or the predicted values for observable quantities like the total energy and dipole moment. However, the NBO representation of the electronic structure is advantageous for visualizing and interpreting the electronic orbitals. NBOs are determined by combinations of hybridized one-center orbitals consisting of familiar Lewis-type forms (*i.e.*, sp, sp^2, sp^3, etc.) and are generally easier to interpret in terms of elementary bonding concepts compared to typical molecular orbitals (MOs). Moreover, the NBO analysis readily permits the assessment of both intramolecular and intermolecular electronic delocalization effects through the population analysis of non-Lewis-type NBOs and a second order perturbation theory analysis of the coupling of between Lewis and non-Lewis-type NBOs. This analysis is especially useful for understanding and quantifying electronic resonance, donor-acceptor coupling (charge transfer), and hydrogen bonding.
28. Otwinowski, Z. & Minor, W. (1997). Methods in Enzymology, Vol. 276, Macromolecular Crystallography, Part A, edited by C. W. Carter Jr & R. M. Sweet, pp. 307–326. New York: Academic Press.
29. G. M. Sheldrick, *Acta Cryst.*, 2008, **A64**, 112.